Vibration Energy Harvesting with Printed P(VDF:TrFE) Transducers to Power Condition Monitoring Sensors for Industrial and Manufacturing Equipment

*Asier Alvarez Rueda, Andreas Petritz, Philipp Schäffner, Markus Postl, Manfred Adler, Maria Belegratis, Jonas Groten, and Barbara Stadlober**

A vibration energy harvesting system based on fully printed piezoelectric transducers is realized. The transducers have a butterfly-like architecture based on two single-optimized cantilevers with a resonance frequency tuned to 49.5 Hz and can be easily mounted to an industrial engine. By comparing single- and multistack configurations of the piezoelectric layers combined with full-wave or voltage doubler rectifiers, the power transfer characteristics and impedance can be matched to the electrical requirements of the sensing circuitry. A single stack with 21 μm thickness results in the maximum power output of 14.4 μW at a vibration velocity of 11.5 mm s^{-1}, typical for industrial engines. The system is used to power a wireless sensor node on a 1 kW rotary pump in normal operation. The system can harvest up to 138 mJ within 24 h, sufficient for daily remote monitoring of the engine's vibration spectrum and temperature state. The system is thus suitable as a low-cost, ecofriendly power source for industrial IoT applications.

1. Introduction

Energy harvesting has been attracting great attention as it holds promise for meeting the sustainability requirements for the upcoming Internet of Things (IoT)[1–4] and Industry 4.0.[5] In many IoT application fields (e.g., condition monitoring in industrial environments), devices must be inexpensive, lightweight, wireless, energy saving, or even self-sustaining in order to simplify installation and maintenance.[6] Currently, most commercial IoT sensors are battery powered and have a limited lifetime. However, in industrial environments, the sensor nodes used for condition monitoring often have to work as standalone units in positions difficult to reach once installed, and thus the use of batteries and in particular their replacement is impractical,[7] especially since it may be deployed in difficult places.[8] A sustainable, ecofriendly, and low-cost alternative to power these devices is by harvesting ambient energy available at the sensor node, which is otherwise just dissipated to the surrounding environment. There are many ambient energy sources, such as solar,[9] radio frequency,[10] temperature gradients,[11] and kinetic or vibrational energy.[12,13] In many cases, a multisource harvesting approach can be an interesting way to boost the energy output.[14]

In this work, we focus on energy harvesting in an industrial environment, in particular harvesting the kinetic energy of vibrations arising from electrically driven engines. In order to convert this kinetic energy into electricity, a triboelectric, piezoelectric, or electromagnetic coupling mechanism can be harnessed. Piezoelectric and triboelectric coupling mechanisms are more suited to make integrated nanogenerators than the electromagnetic one, as they are easier to miniaturize, in exchange of a lower output.[15] Triboelectric nanogenerators (TENGs) became a hot topic after the presentation of flexible harvesters by Fan et al.[16] and subsequently many developments with relatively complex mechanical setups were presented.[17–20]

In contrast to TENGs, piezoelectric nanogenerators (PENGs) have the advantage of being simple in design as they do not require a controlled and reproducible contact between two surfaces in order to function.[21] Usually these generators are realized of piezoceramic materials, which excel in a high intrinsic energy conversion efficiency.[22,23] However, these are brittle and in case of the best-performing lead-based ceramics even pose a risk to the environment.[24] A lead-free and flexible alternative are the ferroelectric polymer poly(vinylidene fluoride) (PVDF), and the printable ferroelectric copolymer poly(vinylidene-trifluoroethylene) (P(VDF:TrFE)). P(VDF:TrFE) can be processed on cheap, flexible, and lightweight substrates such as PET using large-area, scalable printing techniques, enabling a customized design for specific requirements.[25] Although it has significantly lower intrinsic piezoelectric coefficients and conversion efficiency than its ceramic counterparts (d_{33} around 30–35 pCN^{-1}

A. Alvarez Rueda, A. Petritz, P. Schäffner, M. Postl, M. Adler, M. Belegratis, J. Groten, B. Stadlober
MATERIALS – Institute for Sensors, Photonics and Manufacturing Technologies
JOANNEUM RESEARCH Forschungsgesellschaft mbH
Franz-Pichler-Straße 30, 8160 Weiz, Austria
E-mail: barbara.stadlober@joanneum.at

The ORCID identification number(s) for the author(s) of this article can be found under https://doi.org/10.1002/adem.202302140.

DOI: 10.1002/adem.202302140

compared to PZT's 300 pCN^{-1}),[25,26] the ease of processing, mechanical robustness, and potential for large-area fabrication and high integration density can outweigh this intrinsic deficiency in many application fields. Here, we prove the viability of these printed devices as power sources for IoT sensor nodes.

Godard et al. demonstrated a vibration PENG based on a cantilever with printed polymer multilayers.[27] Its remarkably high power output of about 1 mW was achieved using input vibrations with acceleration as high as 5.8 G at 33 Hz. This was done using a shaker. In a real environment, many vibration sources that can be used for energy harvesting generate much lower acceleration values, as shown in Figure S1, Supporting Information. In other studies, the acceleration values might be more realistic, but the frequency they are tuned to is rather high for industrial settings.[28] A more realistic scenario, according to ISO 10816,[29] considers lower vibrational velocities around 5 mm s^{-1} root mean square (RMS) for small pumps and frequencies in the range of 20–60 Hz. If we suppose a main vibration frequency peak at 50 Hz, it corresponds to acceleration RMS value of around 1.6 m s^{-2}. When the PENG is used to power a sensor electronics including wireless transmission, one needs to further consider the voltage requirements and operating range. In literature, piezoelectric harvester systems can be found with output power ranges from few μW to 2 mW, with operating frequencies from very low frequency (0–10 Hz) to several kHz.[30] A comparison of the efficiency of these systems is not straightforward as the excitation conditions are different, like vibration velocity, frequency, size of harvester, etc. An overview of the output powers and operation conditions can be found in ref. [30].

In this work, we demonstrate an energy-autonomous condition monitoring with an energy harvesting system (EHS) that provides the power for a sensing chip (SC), as shown in **Figure 1**. The SC can be used to monitor the temperature and vibration of motors for timely diagnosis of potential problems. As a realistic scenario for condition monitoring, we choose to monitor a rotary pump that generates the vacuum of a high-vacuum (HV) chamber.

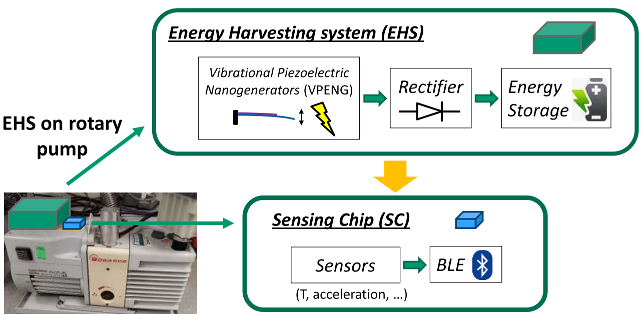

Figure 1. Energy-autonomous condition monitoring for electric motors. It harvests vibrational energy in industrial environments with an EHS to power SC. The EHS consists of VPENG, a rectifier circuit, and an energy storage device. The SC collects the temperature and vibration spectrum of an electric engine for condition monitoring and failure diagnosis. The collected data is sent to some gateway or computer via BLE.

2. Results

2.1. Vibrational Piezoelectric Energy Nanogenerator (VPENG)

The key element of the EHS system in our sensor node is the vibrational PENG (VPENG). The VPENG has the form of two cantilevers in a butterfly-like arrangement with a clamping region in the center. It consists of a piezoelectric transducer printed on top of a polyethylene terephthalate (PET) substrate. The transducers are made of the ferroelectric copolymer P(VDF:TrFE) sandwiched between screen-printed PEDOT:PSS electrodes. The design of the transducer as well as images of the two vertical layer configurations are depicted in **Figure 2**. In the "single" configuration, a single electrode pair is used and 1–3 layers of the piezoelectric polymer are printed on top of each other to obtain different stack thicknesses. In the "multi"-configuration, two stacks of the transducers are printed, where the electrodes are connected in an interdigital manner to connect the vertically aligned stacks in parallel. Figure 2b shows the scanning electron microscopy (SEM) images of cross sections of two devices printed according to the different stack configurations. The shown device with single configuration has three layers of P(VDF:TrFE) printed on top of each other resulting in a maximum stack thickness of 20.8 μm. The multidevice features two

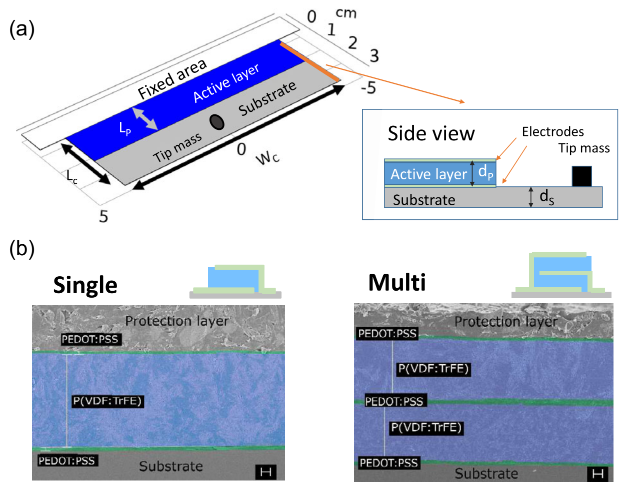

Figure 2. a) Geometry of the VPENG, showing one half of the butterfly-like arrangement and the central clamping (fixed) area. The length L_c, width W_c, substrate thickness d_s, and piezoelectric layer thickness d_p of the cantilever, together with the tip mass M , must be adjusted so that the eigenfrequency of the cantilever matches the vibration frequency of the targeted system. In this scheme, the active layer area is the area where the piezoelectric transducer is present in either of the two stacking configurations. This layer covers the substrate over a length L_p, which must be adjusted to maximize the transducer's power output. An image of the printed harvester is shown in Figure 6. b) Schemes and representative SEM images of transducers with the two different layer stacks (scale bar: 2 μm). The single stack consists of one layer of P(VDF:TrFE) sandwiched between electrodes. In the multistack arrangement, another electrode is added in-between and the two stacks are electrically connected in parallel. PET was used as substrate material, while the electrodes were printed with the conductive polymer PEDOT:PSS. A protective coating was applied on top of the transducers. SEM images were colorized to highlight the different layers of the fully printed transducers.

Table 1. Overview of samples, including their thickness, poling voltage, and remnant polarization.

Sample	Number of stacks	Thickness per stack [μm]	Peak poling voltage [V]	Remnant polarization [mCm^{-2}]
Single-1	1	6.5	700	67.4
Single-2	1	13.1	1350	64.2
Single-3	1	20.8	2000	64.3
Multi	2	13.4	1350	62.0

transducer stacks, each with a double layer of P(VDF:TrFE) and a thickness of 13.4 μm. **Table 1** summarizes the fabricated and tested devices following both configurations, indicating the thickness of the piezoelectric stacks and the number of stacks in the multiconfiguration.

Since the polar domains of the as-prepared screen-printed semicrystalline ferroelectric films are randomly oriented, they have to be aligned in an external electric field larger than the material's coercive field E_c. This process is called "poling" and is described in detail in the Experimental Section. During poling, a macroscopic remnant polarization P_r is built up, which is proportional to the piezoelectric constants d_{ij}[31] and, thus, as a main figure of merit is a measure for the transducer's sensitivity (required for both sensing and harvesting).[32] Representative $D(E)$ poling hysteresis curves of a single- and multistack sample are shown in Figure S2, Supporting Information, where the positive-up negative-down (PUND) procedure was applied to obtain the switching polarization $P(E)$ from the recorded electric displacement D.[33]

The obtained remnant polarization values P_r for the different transducers configuration are summarized in Table 1. An average polarization of $64 \pm 2\,\text{mCm}^{-2}$ was achieved. With the multistack configuration, it has to be noted that although the footprint area of the device is the same as with the single-stack configuration, the electrode area is doubled. This way, a higher charge

generation and thus a higher current output can be achieved with the same transducer area, as will be shown later.

As a resonating system, the cantilever's resonance frequency must be fit to the main vibration component in order to achieve efficient energy conversion. In our demonstration, it is the vibration of a rotary vacuum pump driven by an electric engine. The vibration frequency of an electric motor will be close to its rotation speed, which is a function of the input current frequency (often net frequency) and the number of poles.[34] In Europe, that means the typical target frequency will be close to 50 or 25 Hz, reduced by the rotor slip under load condition. Our targeted system for energy harvesting with our VPENG is a rotary pump with a peak acceleration at around 49.5 Hz as measured with a laser Doppler vibrometer. Finite element model (FEM) simulations and experiments were carried out to optimize the cantilever geometry for harvesting from this vibrational source.

2.2. Parameter Study from FEM Model

FEM simulations were performed to investigate the vibration modes of the VPENG cantilevers for the different geometry parameters and with adding a tip mass. The geometry is shown in Figure 2a. The eigenfrequency of the transducer, which needs to match the motor's main vibration frequency, depends on the cantilever geometry parameters including the length L_c, width W_c, substrate thickness d_s, and piezoelectric layer thickness d_p. It can be further tuned by adding a tip mass M to the edge of the cantilever. **Figure 3** shows the simulated eigenmodes of a cantilever with the normalized z-direction strain component and a point tip mass located at 1 mm from the tip.

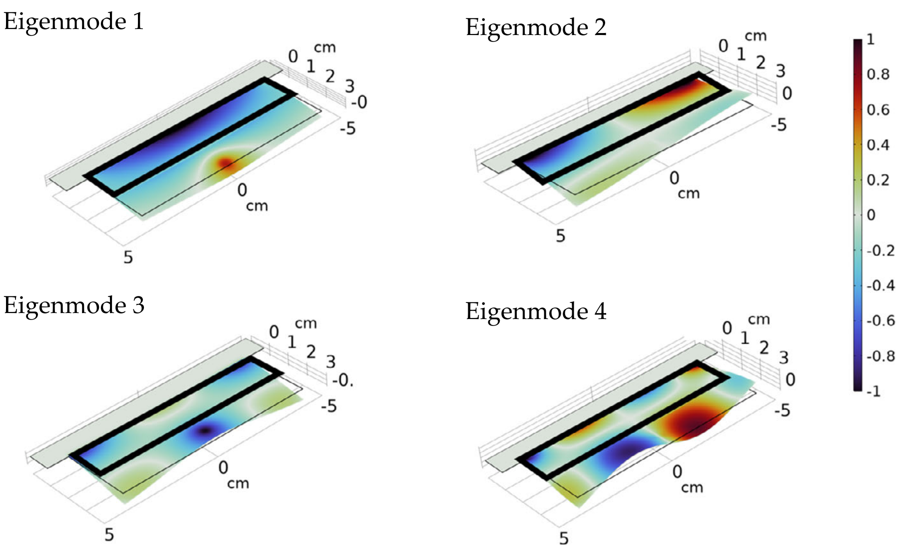

Figure 3. Simulated eigenmodes of a cantilever with $L_c = 30$ mm, $W_c = 8$ cm, $L_p = 16$ mm, a PET substrate with $d_s = 175$ μm, and a point tip mass M of 0.2 g. The geometry is the one shown in Figure 2. The color scale represents the strain component on the Z direction, normalized to the maximum value for each eigenvalue. The thin black lines indicate the initial geometry, while the thick rectangle remarks the active area, in which is the area covered by the piezoelectric material (characterized by length L_p). The colored deformed layer shows the shape of the mode as well as the sign of the local strain (>0: tensile strain, <0: compressive strain). The displacement is scaled up for visualization purposes.

The active, piezoelectric layer couples the local strain with the material polarization and is characterized by the length L_p. On the physical samples, this layer consists of PEDOT:PSS electrodes sandwiching the P(VDF:TrFE) layer, either in a single- or multistack configuration as described above. In the simulation, the electrodes are only included as boundary conditions for the voltage field, while P(VDF:TrFE) is implemented as an orthotropic linear elastic piezoelectric material, as shown in previous works.[35,36] The change in local piezoelectric polarization, and therefore surface charge density, is proportional to the local strain component parallel to the poling direction (z-direction). Thus, in order to avoid charge cancelations, the strain field amplitude must have the same sign in the area covered by the electrode (~defined by L_p). We can see that this is true for a cantilever working in the fundamental mode (eigenmode 1, blue area) as shown in Figure 3. At higher modes (eigenmodes 2–4), the presence of compressive and tensile strains in z-direction (red and blue regions) generates piezoelectric charges of opposite sign, resulting in partial surface charge cancellation in the active transducer area. Thus, for the higher eigenmodes, more complex electrode designs would be necessary to avoid these cancellation effects, which would make the fabrication process more complicated. To maximize the charge generation and thus the energy output of the VPENG, the optimum transducer active area must be found for each mode of vibration to be used.

Once the substrate material is fixed, the resonance frequency is determined by geometric parameters and tip mass. As shown in **Figure 4**, the main change in resonance frequency comes from the length and substrate thickness of the cantilever. In contrast, the active, piezoelectric layer thickness d_p has a very small effect on the resonance frequency compared to the other parameters. The cantilever width W_c has a moderate effect on the resonance frequency compared to its length L_c. This strong dependence on the cantilever length is expected, since, from beam theory, the fundamental frequency f_r for a rectangular isotropic cantilever follows the relation[37]

$$f_r = \frac{\lambda_r^2}{2\pi}\sqrt{\frac{E_{\text{young}} I}{m L_c^4}} \propto \frac{\sqrt{W_c}}{L_c^2} \tag{1}$$

where m is the mass per unit length of the cantilever, E_{young} is the Young's modulus of the cantilever, and I is the area moment of inertia of the cross section and directly proportional to the beam width W_c. λ_r is the frequency number, which are solutions of the characteristic equation

$$1 + \cos\lambda \cosh\lambda = 0 \tag{2}$$

As mentioned above, another important factor that comes into play for the harvester energy output is the length of the active transducer area L_p.

In **Figure 5**, we calculated the maximum output of transducers with different lengths L_p of active layer at impedance matching conditions for a mass load of 0.22 g on the tip. By setting up short-circuit conditions (voltage difference equal to 0) and open-circuit conditions (charge transfer between electrodes equal to 0), short-circuit current (I_{SC}) and open-circuit voltage (V_{OC}), respectively, were obtained at resonance condition. For doing so, we performed a frequency sweep around the resonant frequency for each length of the active part as shown in Figure 5

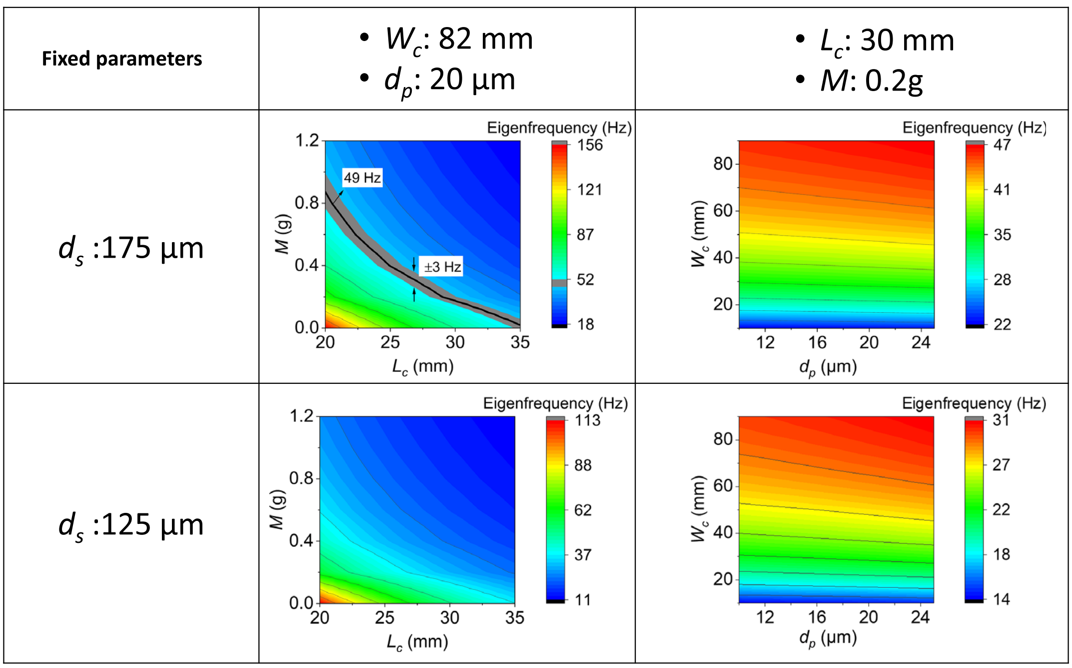

Figure 4. Variation of the simulated eigenfrequency depending on different sets of model parameters. Each panel shows the frequency shift when two parameters are changed, while the other parameters remain fixed. The header indicates the values of the fixed parameters for each row and column, respectively. As we can see, a change of tip mass M and length L_c results in the highest variation of the eigenfrequency. A substrate thickness of 175 µm is necessary in order to achieve the targeted eigenfrequency of 49 Hz for a wide range of tip mass and cantilever length. For the top left panel, the eigenfrequency range of 49 ± 3 Hz is highlighted.

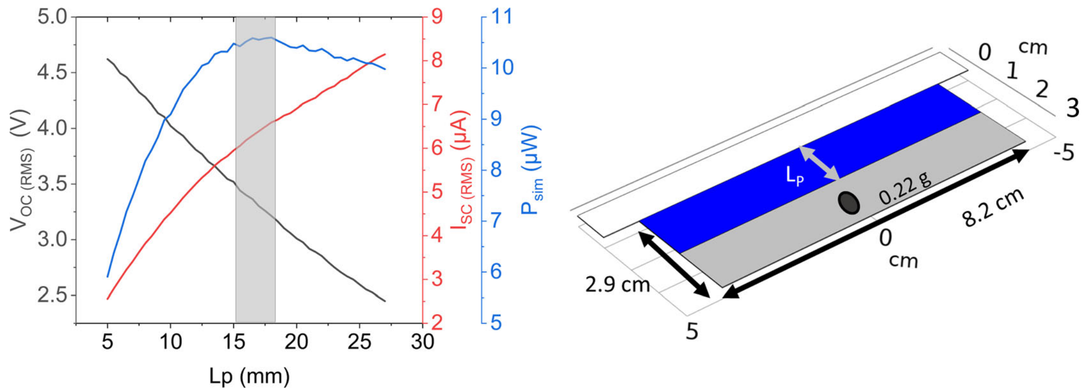

Figure 5. Simulation of short-circuit current $I_{SC\ (RMS)}$ (red line) and open-circuit voltage $V_{OC\ (RMS)}$ (black line) for varying active layer length L_p ($d_p = 20\,\mu m$, $d_s = 175\,\mu m$). The theoretical peak load power P_{sim} (blue line) was calculated as $\frac{1}{2}V_{OC,RMS}*I_{SC,RMS}$, which is the expected power output at impedance matching condition. (The small ripples in the calculated power plot are a consequence of finite mesh sizes of the FEM model.) In the model, the cantilever was excited at its natural frequency, around 49.5 Hz for the different length of the active transducer areas L_p with an acceleration RMS value of $4\ ms^{-2}$. The mass is placed 1 mm from the edge of the cantilever. The range of L_p resulting in maximum power output is indicated in gray in the graph.

and plotted the current and voltage values together with the calculated theoretical output power P_{sim}. With L_p ranging between 1 and 29 mm, the frequency varied only by 2.2 Hz, which may be considered negligible compared to the other tuning parameters. This method introduces some noise on the output since the meshing changes for each length value, introducing numeric errors. Still, the trends are clear, with the short-circuit current (I_{sc}) increasing and the open-circuit voltage (V_{oc}) decreasing with length L_p.

This trend in the electrical output in dependence of L_p can be understood as follows. When the cantilever oscillates in the fundamental mode, the strain is concentrated at the clamped edge. With increasing L_p, more charges are generated from the piezoelectric response due to bending strain, meaning an increased current in the dynamic response. However, the strain amplitude decreases along the cantilever length direction, causing a flattening of the slope in the current trend. Furthermore, in the vicinity of the tip mass, the deformation causes even an inverse strain response (normalized z-strain > 0 in Figure 3). Consequently, for high L_p (>18 mm), that is, when the piezoelectric layer edge approaches the tip mass position, the locally generated surface charges have opposite polarity and diminish the total charge amount and current response. These two effects cause a decrease of slope in the short current curve of Figure 5.

With regard to the voltage output, the trend is related to both the generated charges Q and the transducer's capacity.

$$V_{OC} = \frac{Q}{C_p} \tag{3}$$

While the capacity grows with area and therefore proportional to L_p, the generated charge does not increase equally for the factors mentioned above. Thus, the voltage output of the transducer will reduce with increasing L_p, as shown in Figure 5. The maximum power output is achieved for an electrode length roughly half of the cantilever length (L_p between 15 and 18 mm).

According to this, a cantilever of 29 mm length and 82 mm width can be tuned to a fundamental frequency of around 49 Hz with a mass of just 0.22 g fixed slightly (1 mm) inward the cantilever edge. This way, the transducer's eigenfrequency would match the fundamental frequency of a rotary pump, as shown in Figure S1, Supporting Information, and is measured with a laser vibrometer. A transducer's active layer length L_p about half the length of the cantilever is expected to deliver maximum power output. In contrast, a shorter cantilever may reach the same resonance frequency with higher mass, but the power output will be reduced due to the smaller active transducer area.

2.3. Electrical Output Performance of the VPENGs

In order to investigate the frequency-dependent sensing/harvesting properties of the VPENGs, we integrated the transducers into a 3D-printed protective housing, which also provides a mechanism to clamp the transducers, see **Figure 6**a. This VPENG box was then mounted on an electromagnetic shaker to simulate a vibrating machine, as shown in Figure 6a. The tested VPENGs were tuned to a fundamental frequency of 49 Hz by adjusting the geometry and tip mass to the values obtained from simulation. A sinusoidal vibration with an RMS acceleration of $4\ m\,s^{-2}$ was applied, which corresponds to RMS velocity of $11.5\ mm\,s^{-1}$. In Figure 6b the output power P_{out} of the different transducer configurations is plotted as a function of load resistance R_L.

The harvesters showed a maximum power output range from 4 to 14 µW at an optimum load between 0.5 and 1 MΩ. The power output values, including the peak power, the open-circuit voltage (V_{OC}), and short-circuit current (I_{SC}), are summarized in Table S1, Supporting Information. From Figure 6 and Table S1, Supporting Information, we can see that the output power is increased for thicker layers of the piezoelectric material (red curves, Single-1 to Single-3), which can be attributed to the enhanced output voltage level V_{OC}. According to Equation (3), the voltage scales inversely with the capacitance and thus proportionally to the layer thickness, whereas the piezoelectric charge is caused by the bending strain, which hardly varies with the layer thickness. The device with multistack approach (Multi-1) delivers

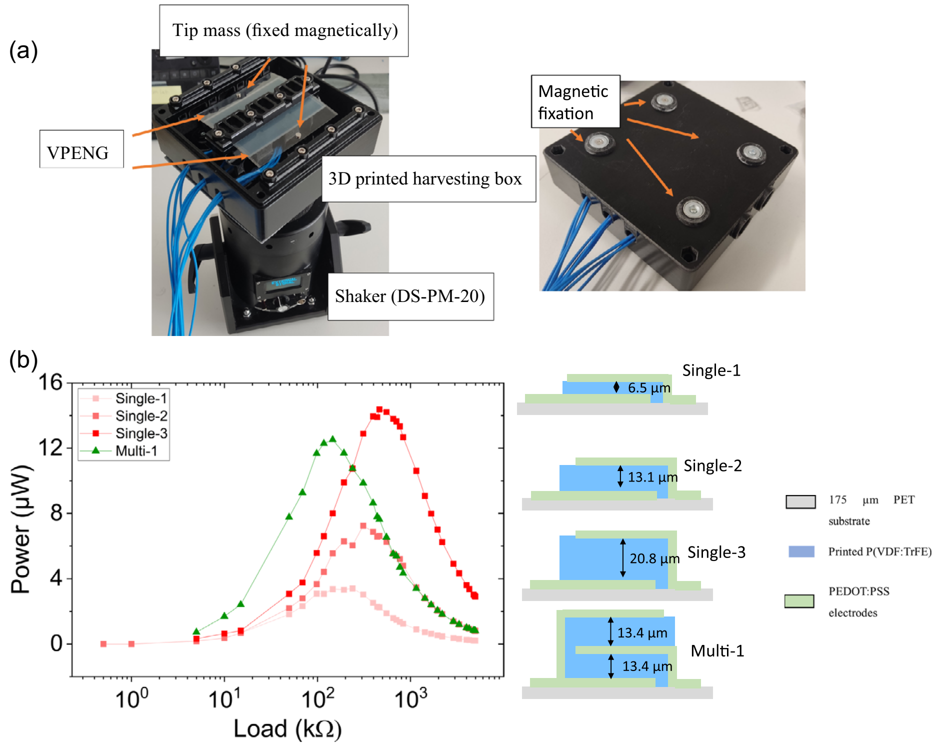

Figure 6. a) EHS with cantilevers mounted to the clamp mechanism integrated in a 3D-printed housing. The EHS can be placed either on a shaker for controlled excitation and characterization (left) or fixed to the chassis of the rotary pump via integrated magnets (right). For systematic excitation, the shaker applied a sinusoidal displacement, where the frequency was swept from 0 to 100 Hz and the RMS acceleration ranged from 0 to 15 $\mathrm{m\,s^{-2}}$. The acceleration was measured with a single-axis accelerometer (not visible on the image). The tip mass allows to adjust the resonance frequency to 49 Hz. b) Power curve of VPENGs operating at a 49 Hz sinusoidal vibration with an RMS acceleration of 4 $\mathrm{m\,s^{-2}}$, which corresponds to a RMS velocity of 11.5 $\mathrm{mm\,s^{-1}}$. The stacking configuration and piezoelectric layer thickness is shown on the right. In all cases, $L_c = 29$ mm, $W_c = 82$ mm, $M = 0.22$ g. The eigenfrequency was tuned by adjusting the tip mass position.

approximately twice the current compared to the single stack with the same active layer thickness (Single-2) while the open-circuit output voltage is the same for both devices. As shown in Figure 6b, the power output is roughly doubled. It can be also noted that the peak power for Single-3 is slightly higher than the one simulated in Figure 5, even though they should be similar. The simulated value is 10.6 μW compared to the experimental 14.4 μW. Both, the simulated short-circuit current and open-circuit voltage, are smaller than the experimental ones, which may be due to an underestimated damping factor in the simulation. The values are compared in Table S1, Supporting Information.

The open-circuit voltage level of the VPENG has to be high enough to reach the requirements of the electronics it must power. A commercial energy harvesting chip like LCT 3588-1 from Analog Devices has an input voltage range of 2.7–20 V.[38] The used prototype sensor chip platform from Infineon is able to operate down to 1.5 V. However, higher open-circuit voltage levels are preferred to achieve higher energy stored in a capacitor. Thus, in view of energy storage with a capacitor, a thicker layer might be preferred in order to achieve a higher voltage level. As shown in the next section, the right choice of the rectifier circuit is also important to optimize the energy harvesting condition.

2.4. Performance of Vibration Energy Harvesting on a Rotary Pump

After studying the power output of the VPENGs in a simulated environment, the harvesting capability of the EHS was tested in a more realistic setting. For doing so, we harvested the vibration energy of a rotary pump. This rotary pump with a nominal power of 0.55 kW generates the vacuum of a high vacuum (HV) chamber in our lab and is shown in Figure S3, Supporting Information. This pump operates nonstop in order to hold the required vacuum level in the chamber (apart from venting of the chamber and sample loading) and thus provides a continuous source of vibration to harvest.

The harvested energy was measured by monitoring the voltage level of a storage capacitor connected to a rectifier (cf. Figure 1). Figure S3, Supporting Information, shows an image of the setup and the electric diagram. The EH box was magnetically attached to a magnetic metal sheet that was glued with the two-sided scotch tape to the carcass of the motor. The vibration spectrum of the motor-driven pump was measured at a steady state with a laser Doppler vibrometer and a peak velocity of 4.6 $\mathrm{mm\,s^{-1}}$ was found at 49.5 Hz, which corresponds to around 1.4 $\mathrm{m\,s^{-2}}$. When the chamber is opened and closed again, the vibration increases slightly during evacuation of the chamber due to the increased workload on the pump. The vibration in this case varies between of 4.5 mm s^{-1} and 6.7 mm s^{-1}. After around 15 min, the motor reaches the steady state. The eigenfrequency of the VPENG was fine tuned to the vibration frequency by slightly adjusting the tip mass position in situ. The VPENG was connected to a rectifying circuit, which was either a voltage doubler (VD) or a full-wave rectifier (FWR) and feed a 4.7 mF storage capacitor; see Figure S3, Supporting Information. In order to test just the harvesting capabilities, the condition monitoring chip was not connected and the storage capacitor was charged until reaching the saturation voltage (V_{sat}) that was dependent on the V_{OC} of the used VPENG and type of rectifier. The stored energy E_S (Equation (4)) and output power P_{EH} (Equation (5)) of the EHS can be derived from the storage capacitance C and the voltage V_c measured at the capacitance.

$$E_S = \frac{1}{2} C V_c^2 \tag{4}$$

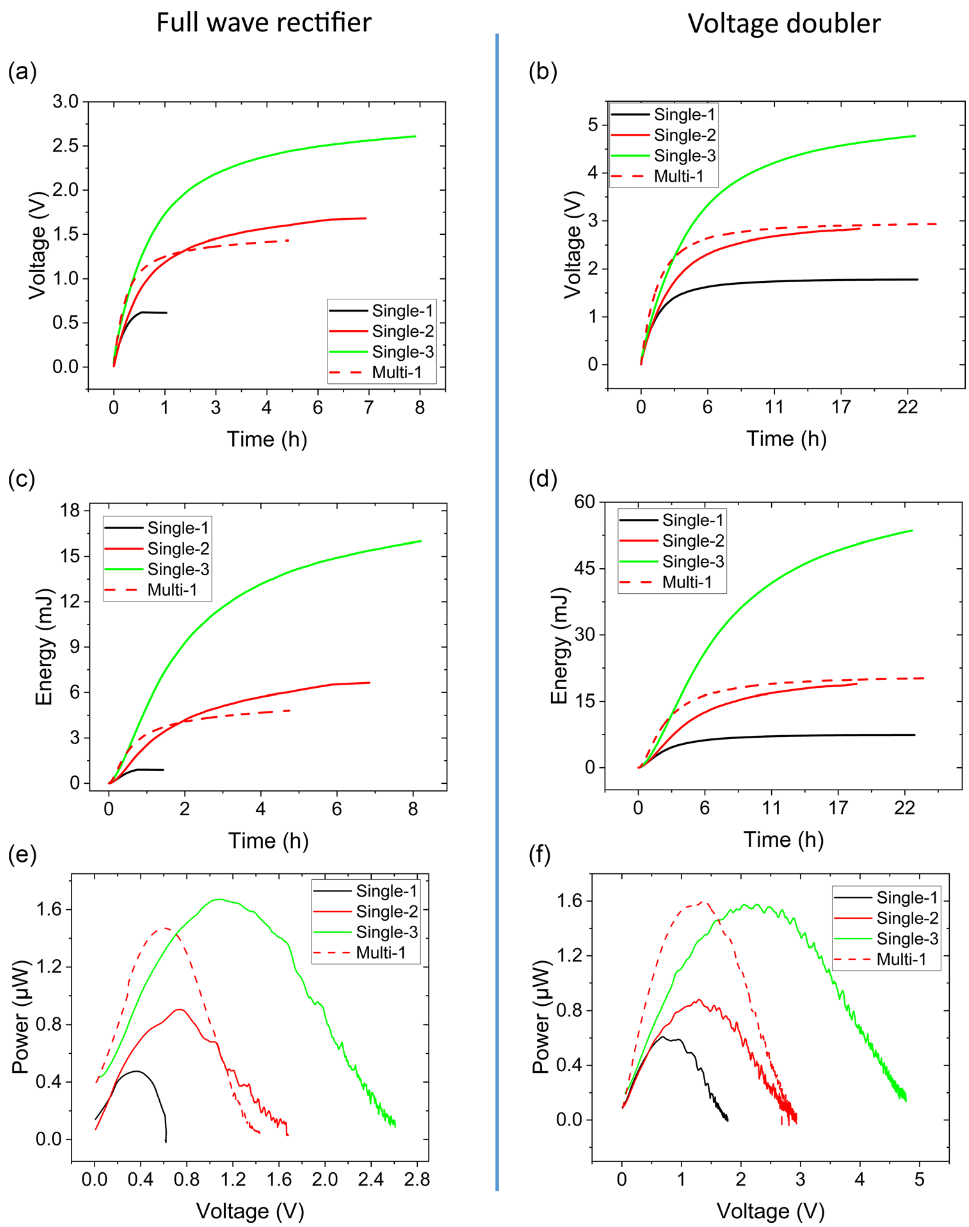

Figure 7. Harvesting the vibration energy of a rotary pump at 49.5 Hz. a,b) Capacitor voltage and c,d) stored energy when using FWR or VD as rectifier circuit ($C = 4.7$ mF). The VD clearly offers higher output voltages as expected. For samples Single-2 and Multi-1 with similar thickness of the piezoelectric layer, the saturation voltage is comparable; however, the energy transfer at lower voltage levels is noticeably better with the Multi-1 configuration. The overall energy transfer is significantly higher when using a VD as compared to the FWR. e) and f) Transferred power versus voltage according to Equation (5). With the VD, a high transfer power can be maintained over a large voltage range. A Savitzky–Golay filter with a 100-point window was applied to filter the high-frequency ripple in the voltage plot.

$$P_{\mathrm{EH}} = \frac{\mathrm{d}E_S}{\mathrm{d}t} \tag{5}$$

Since the power is calculated from the voltage stored in the capacitor, it accounts for all losses occurring during rectification.

Figure 7 summarizes the measured output energy and power of the EHS with different VPENGs and rectifiers. It is evident that thicker piezoelectric layers lead to higher saturation voltage levels, as we can see in Figure 7a,b. Sample Single-3 shows the highest output with voltage levels of 2.6 and 3.8 V for the FWR and VD, respectively, after a duration of 8 h. Comparing the two rectifier types, one observes that within the same time window more energy is harvested with the VD compared to the FWR. The output peak power, though, is slightly higher for the FWR, but concentrated in a small window at lower voltage levels, as revealed in Figure 7e,f. For the sake of completeness, Figure S5 and S6, Supporting Information, show the power output versus time. These plots indicate that though the VD circuit allows for higher harvested energy, the FWR is more efficient at the onset of charging.

Next, we can compare the two VPENG configurations with similar active layer thickness per stack, that is, Single-2 and Multi-1. As expected, the achieved saturation voltage levels are comparable. However, from Figure 7c,d one can see that the Multi-1 has a better energy transfer at lower voltage levels compared to the Single-2. By inspecting the power, as shown in Figure 7e,f, we realize that the harvesting peak power is roughly doubled with the stack connected in parallel, providing higher current levels. When the output voltages needed for powering a user electronics are well below the saturation voltage, shorter harvesting times can thus be achieved with the multiconfiguration.

To power the SC, a high enough voltage level is necessary. The integrated sensor chip used in this test requires minimum 1.5 V to operate, so the available energy is at most $\Delta E = C(V_{\mathrm{sat}}^2 - (1.5\mathrm{V})^2)$. From previous tests, we see that sample Single-3 can reach the highest voltage levels. Thus, it is the most suited sample for powering the SC. To increase the available energy for powering the chip, we used four 4.7 mF capacitors in parallel, giving a total storing capacity of 18.8 mF. When repeating the charging with a FWR, a capacitor voltage of 3.15 V was achieved after 24 h, close to the saturation voltage. This voltage corresponds to 92.5 mJ of stored energy. The charging characteristics of this run are summarized in supplementary Figure S4, Supporting Information. The peak charging power was 2.7 μW and was reached after 2.5 h of charging when the voltage level was about 1.5 V. It must be remarked that this value differs from the one on Figure 7 due to different storing capacities.

Once the charging was complete, the condition monitoring chip was connected. This operation is shown in the Video 1, Supporting Information. Monitoring the energy consumption by the chip, as plotted in **Figure 8**, reveals that the most energy-expensive operation is the chip wakeup, consuming 26 mJ with a peak power of 9 mW. Afterward, it requires around 3 mJ to connect with the PC via Bluetooth low energy (BLE) and around 2 mW to perform continuous measurements. After 20 s

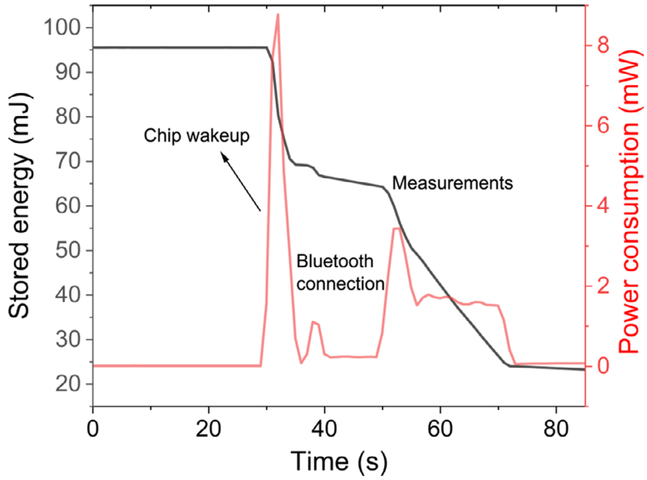

Figure 8. Power consumption of the SC and the energy stored in the capacitor. During operation, it can measure the temperature, the pressure, and the acceleration on the pump. The chip also has the possibility to measure a voltage level. The capacitor voltage was monitored with an electrometer. An example of a measurement is presented in Video 1, Supporting Information.

of measurement, the cap voltage dropped to 1.5 V, forcing the chip to shut down.

Using this same setup, we performed a stability test. For this test, the transducer was operated continuously for 50 h at realistic vibration conditions (on rotary motor), which corresponds to around 8.82 million bending cycles at a resonance frequency of 49 Hz. After this 50 h continuous operation, we did another 50 h run. There was no significant change in the output power and the voltage level of the storage capacitor between both runs, as shown in Figure S6a,b, Supporting Information, respectively.

Finally, we used a combination of FWR and VD for enhanced energy harvesting adopted to the needed voltage levels and energy transfer characteristics of the two rectifier types. Since the sensor chip's minimum operation voltage is 1.5 V, which coincides with the peak power value of the FWR, we used a FWR to charge the capacitor up to this voltage, which took 3 h. Then, a VD replaced the FWR in order to achieve higher voltage values and thus higher maximum energy levels within the same total time. The charging curve, as depicted in **Figure 9**, is smooth, apart from a small discontinuity during circuit exchange. The saturation voltage is higher for the combined approach, and thus more energy is transferred into the capacitor within the same time. A comparison of the power output between the two experiments (FWR only vs. FWR + VD) in Figure 9b reveals that the energy transfer is high with the FWR after complete discharge of the capacitor, but drastically drops after reaching its power peak after 3 h. The exchange to the VD ensures that the power remains at a high level for a longer time. With this combination, an energy level of 138 mJ was reached after 24 h, which is 43.8% more than when using solely a FWR circuit. This result suggests that for standalone sensor nodes with noncontinual operation, that is, with frequent full discharge of the storage capacitor, a power management circuit that switches between FWR and VD configuration might increase the

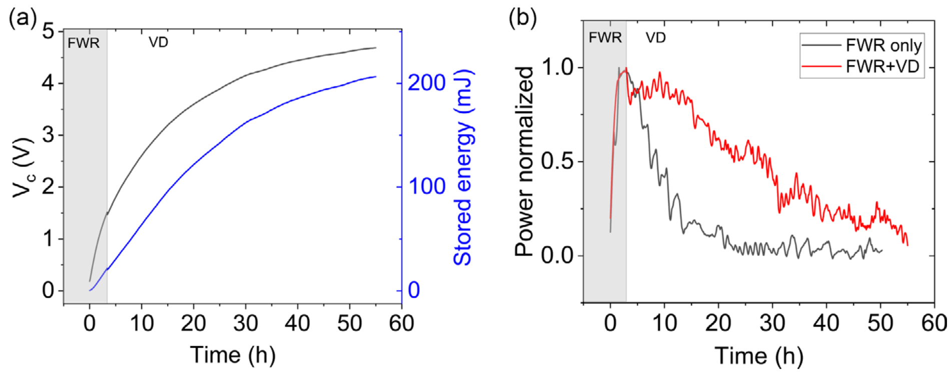

Figure 9. Enhanced energy harvesting using a combination of FWR and VD for improved impedance matching. In the initial charging phase, FWR was applied, which was then replaced by a VD to obtain a higher voltage, that is, energy level. a) Voltage and energy plot. The rectifier circuits were exchanged at a level of 1.5 V, marked by a small discontinuity in the graph. b) Charging power comparison between only using FWR and using the combination of circuits. For the FWR alone, the power drops quickly after reaching its peak, while with the FWD + VD combination a much better overall energy transmittance is achieved. (The power was normalized to the respective peak power to compensate for variations in the machine vibration between the two measurement runs.).

overall energy harvesting performance. We understand that further research is required to test the practicality of this concept.

3. Conclusion

In this work, we demonstrated vibration energy harvesting with fully printed PENGs under realistic vibration conditions. Single- and multistacking configurations of the VPENGs were evaluated in combination with full-wave or VD rectification circuits at around 50 Hz. The geometry was optimized with FEM simulations, revealing a maximum power output when the piezoelectric layer covers about half the length of the cantilever with a single-tip mass. A maximum power output of 14.4 μW at 11.5 mm s^{-1} RMS vibration velocity and 49 Hz was obtained experimentally. When tested on a rotary vacuum pump in the application for self-sustained condition monitoring of the driving motor, a peak power of 1.6 μW was achieved during energy storage, for a vibration of 4.6 mm s^{-1}. Here, a single stack with a thicker active material is preferred to achieve higher saturation voltage levels, whereas a parallel connection of two stacks enables faster charging at the onset at low voltage levels. The overall energy transfer after 6 h was 25 mJ when using a VD for rectification, which was 66% more than the value achieved with FWR at the same harvesting condition.

The EHS was able to power a condition monitoring chip after harvesting the vibrations of a rotary pump over 24 h. With the stored energy of 93 mJ, the SC could power up, establish a Bluetooth low-energy connection, and perform measurements plus wireless data transmission for around 20 s. The EHS can thus be directly applied to monitor engines with a more or less constant peak vibration frequency during operation, such as pump or fan drives.

Finally, our study suggests that a combination of a FWR and a VD could be of advantage to speed up the charging after full discharge of the storage capacitor by switching from a FWR to a VD circuit once a low threshold voltage is achieved. With this strategy, the time necessary to harvest the required energy level for initiating the measurement was reduced from 24 h to 15 h compared to using a FWR only.

4. Experimental Section

VPENG Fabrication: The VPENG consists of a polyethylene terephthalate (PET) substrate cantilever with the piezoelectric transducer screen printed on top, following the procedure described in another stidy.[39] The electrodes were printed with PEDOT:PSS ink (Celvios SV4), while for the piezoelectric layer we used FC-20 powder from Arkema (monomer ratio of VDF:TrFE = 80:20), dissolved in gamma-butyrolactone. The electrical connection lines were printed with Bectron CP 6612 silver ink. For the single- and multistack samples, several layers of the P(VDF:TrFE) ink were printed until the desired thickness indicated in Table 1 was achieved. The single-stack transducers had 1–3 piezoelectric layers sandwiched between the PEDOT:PSS top and bottom electrodes. For the multistack configuration, another electrode design was used. Here, the bottom and top electrodes were printed with the same screen and electrically connected. The second, intermediate electrode was printed after two piezoelectric layers, followed by another two piezoelectric layers to achieve electrical parallel connection. A schematic representation of the device's layer configuration is already shown in Figure 6b.

Electrical Poling Step: A sinusoidal voltage with a frequency of 1 Hz was applied via the printed connection lines. The amplitude ranged from 700 to 2000 V depending on the thickness of the piezoelectric layer. We started with a low amplitude, and it was increased in successive poling steps until a saturation of polarization was achieved. At the end of the poling, PUND sequence was applied, thus obtaining the remnant polarization of the piezoelectric layer.[33]

FEM Model: An FEM model of the cantilever was implemented in COMSOL, where only the substrate and the active layer were considered as active physical domains. The substrate was modeled as an isotropic liner elastic material, while the piezoelectric layer used an orthotropic model with COMSOL's in-built piezoelectric coupling equations following our previous works.[35,36]

An isotropic damping parameter of $\eta = 0.015$ was used to obtain realistic values at resonance. As electrical boundary conditions, the voltage at bottom was set to 0 V. On the top boundary, a terminal boundary condition was set. This boundary condition allows two modes depending of which quantity is set: voltage and charge mode. In voltage mode, the terminal was set to 0 V to simulate short-circuit conditions. The charge was then calculated as the integral of the displacement vector over the boundary area. Similarly, in charge mode the charge was fixed equal to 0C to simulate open-circuit conditions. This condition allows to solve the electrostatic equation and retrieve the voltage at the boundary.

Energy Harvesting and Vibration Tests: For testing, the harvesting transducers were fixed to a 3D-printed protective box, as indicated in Figure 6a. The box was 3D printed with an Objet30 pro V2 3D printing machine using a Alphacam VeroBlackPlus photopolymer filament. The box clamps the transducer sheet in the middle, allowing both sides to oscillate like a butterfly. It also houses magnets in the bottom of the box to ease attachment to magnetic surfaces like machinery, as shown in the same figure.

The transducers were tested using a Dewesoft DS-PM-20 electromagnetic shaker with a sinusoidal drive signal from a Dewesoft Sirius DAQ. We measured the power output by connecting the transducer to a probe resistor and measuring the voltage drop with the same DAQ unit. The input impedance of the measurement channel was 10 MΩ. It must be considered then that the actual load resistance connected to the transducer is the parallel equivalent resistance between input impedance and probe resistor. With these parameters, current and power can be derived, respectively:

$$I_{rms} = \frac{V_{rms}}{R} \tag{6}$$

$$P_{ave} = \frac{V_{rms}^2}{R} \tag{7}$$

where V_{rms} is the RMS of the voltage signal and R is the load resistance.

For the energy harvesting tests, we connected the harvesting transducers to the rectifier circuit (FWR or VD) and a capacitor. The capacitor voltage was measured with a Keithley 6517 A electrometer. From the voltage value, stored energy and charging/consumed power were calculated via Equation (4) and (5). The rotary pump was a D16 BCS PFPE model from Trivac. The utilized Infineon chip was a prototype sensing platform module, not available commercially. During operation, temperature, acceleration, and pressure was measured. The chip had also the possibility to measure voltage, but it was not used on the experiment. The sampling rate of the chip was 0.8 Hz, and thus too low for vibration detection, but enough to monitor the temperature of the pump itself.

Supporting Information

Supporting Information is available from the Wiley Online Library or from the author.

Acknowledgements

The authors thank the team from Infineon Technologies Austria AG for providing the integrated SC. This work was done as part of the projects SYMPHONY and ELENA. The project SYMPHONY received funding from the European Union's Horizon 2020 research and innovation programme under grant agreement no. 862095. The ELENA project was funded by the Austrian research promotion agency (FFG) under project number 871747.

Conflict of Interest

The authors declare no conflict of interest.

Author Contributions

A.A.R. conducted investigation, validation, formal analysis, writing the original draft, and visualization. A.P. conducted investigation, conceptualization, methodology, and writing the review and editing. P.S. conducted conceptualization, methodology, and writing the review and editing. M.P. and M.A. took care of resources. M.B. took care of investigation. J.G. took care of resources, project administration, funding acquisition, and supervision. B.S. conducted supervision and funding acquisition.

Data Availability Statement

The data that support the findings of this study are available from the corresponding author upon reasonable request.

Keywords

condition monitoring, P(VDF:TrFE), screen printing, vibration energy harvesting

Received: December 14, 2023
Revised: February 20, 2024
Published online:

[1] T. Sanislav, G. D. Mois, S. Zeadally, S. C. Folea, *IEEE Access* **2021**, *9*, 39530.
[2] D. Ma, G. Lan, M. Hassan, W. Hu, S. K. Das, *IEEE Commun. Surv. Tutorials* **2020**, *22*, 1222.
[3] A. E. Akin-Ponnle, N. B. Carvalho, *Smart Cities* **2021**, *4*, 476.
[4] H. Elahi, K. Munir, M. Eugeni, S. Atek, P. Gaudenzi, *Energies* **2020**, *13*, 5528.
[5] X. Li, D. Li, J. Wan, A. V. Vasilakos, C.-F. Lai, S. Wang, *Wireless Netw.* **2017**, *23*, 23.
[6] Q. Cao, F. Giustozzi, C. Zanni-Merk, F. De Bertrand De Beuvron, C. Reich, *Cybern. Syst.* **2019**, *50*, 82.
[7] F. K. Shaikh, S. Zeadally, *Renewable Sustainable Energy Rev.* **2016**, *55*, 1041.
[8] S. Sharma, R. K. Bansal, S. Bansal, in *2013 Int. Conf. on Machine Intelligence and Research Advancement*, IEEE, Katra, India **2013**, pp. 58–62.
[9] D. Hao, L. Qi, A. M. Tairab, A. Ahmed, A. Azam, D. Luo, Y. Pan, Z. Zhang, J. Yan, *Renewable Energy* **2022**, *188*, 678.
[10] S. Selvan, M. Zaman, R. Gobbi, H. Y. Wong, *J. Electromagn. Waves Appl.* **2018**, *32*, 2110.
[11] Z. Liu, B. Tian, Y. Li, Z. Guo, Z. Zhang, Z. Luo, L. Zhao, Q. Lin, C. Lee, Z. Jiang, *Small 19*, 2304599.
[12] H. Liu, J. Zhong, C. Lee, S.-W. Lee, L. Lin, *Appl. Phys. Rev.* **2018**, *5*, 041306.
[13] L. Dong, A. B. Closson, C. Jin, I. Trase, Z. Chen, J. X. J. Zhang, *Adv. Mater. Technol.* **2019**, *4*, 1900177.
[14] Y. Bai, H. Jantunen, J. Juuti, *Adv. Mater.* **2018**, *30*, 1707271.
[15] Z. L. Wang, *Mater. Today* **2017**, *20*, 74.
[16] F. R. Fan, Z. Q. Tian, Z. Lin Wang, *Nano Energy* **2012**, *1*, 328.
[17] Y. Wang, Y. Yang, Z. L. Wang, *NPJ Flexible Electron.* **2017**, *1*, 10.
[18] Z. Zhao, X. Pu, C. Du, L. Li, C. Jiang, W. Hu, Z. L. Wang, *ACS Nano* **2016**, *10*, 1780.
[19] H. J. Choi, J. H. Lee, J. Jun, T. Y. Kim, S. W. Kim, H. Lee, *Nano Energy* **2016**, *27*, 595.
[20] J. Chen, G. Zhu, W. Yang, Q. Jing, P. Bai, Y. Yang, T. C. Hou, Z. L. Wang, *Adv. Mater.* **2013**, *25*, 6094.
[21] J. Tichý, E. Jirí, E. Kittinger, J. Prívratská, in *Fundamentals of Piezoelectric Sensorics*, Springer, Berlin, Heidelberg **2010**.
[22] S. Srinivasulu Raju, S. B. Choi, M. Umapathy, G. Uma, *Sens. Actuators, A* **2019**, *297*, 111522.
[23] Q.-M. Wang, L. E. Cross, *Ferroelectrics* **1998**, *215*, 187.
[24] P. K. Panda, B. Sahoo, *Ferroelectrics* **2015**, *474*, 128.
[25] B. Stadlober, M. Zirkl, M. Irimia-Vladu, *Chem. Soc. Rev.* **2019**, *48*, 1787.
[26] M. S. Woo, J. H. Ahn, J. H. Eom, W. S. Hwang, J. H. Kim, C. H. Yang, G. J. Song, S. D. Hong, J. P. Jhun, T. H. Sung, *Sens. Actuators, A* **2018**, *269*, 524.

[27] N. Godard, L. Allirol, A. Latour, S. Glinsek, M. Gérard, J. Polesel, F. Domingues Dos Santos, E. Defay, *Cell Rep. Phys. Sci.* **2020**, *1*, 100068.
[28] S. Roundy, P. K. Wright, *Smart Mater. Struct.* **2004**, *13*, 1131.
[29] ISO10816 Charts, http://www.vibsens.com/index.php/knowledge-base/iso10816-iso7919-charts/iso10816-charts (accessed: May 2023).
[30] H. Li, C. Tian, Z. D. Deng, *Appl. Phys. Rev.* **2014**, *1*, 041301.
[31] T. Furukawa, *IEEE Trans. Electr. Insul.* **1989**, *24*, 375.
[32] H. Li, C. R. Bowen, Y. Yang, *Adv. Funct. Mater.* **2021**, *31*, 2100905.
[33] K. M. Rabe, M. Dawber, C. Lichtensteiger, C. H. Ahn, J.-M. Triscone, in *Physics of Ferroelectrics*, Springer, Berlin, Heidelberg **2007**, pp. 1–30.
[34] M. J. Costello, in *Proc. of the 19th Turbomachinery Symp.*, Texas A&M University, Turbomachinery Laboratories, USA **1990**.
[35] A. Alvarez Rueda, P. Schäffner, A. Petritz, J. Groten, A. Tschepp, F. Petersen, M. Zirkl, B. Stadlober, *Sensors* **2023**, *23*, 603.
[36] P. Schäffner, M. Zirkl, G. Schider, J. Groten, M. R. Belegratis, P. Knoll, B. Stadlober, *Smart Mater. Struct.* **2020**, *29*, 085040.
[37] C. V. Dung, E. Sasaki, *Sensors* **2016**, *16*, 601.
[38] LTC3588-1 Datasheet and Product Info | Analog Devices, https://www.analog.com/en/products/ltc3588-1.html#product-overview (accessed: January 2024).
[39] H. Fares, L. Seminara, L. Pinna, M. Valle, J. Groten, M. Hammer, M. Zirkl, B. Stadlober, in *Proc. IEEE Int. Symp. on Circuits and Systems*, Florence, Italy **2018**.

